Draft version September 22, 2016
Preprint typeset using LaTeX style AASTeX6 v. 1.0

KAVLI 2016 PROJECT:
INFLUENCE OF PLANETARY OBLIQUITY ON ATMOSPHERIC DYNAMICS ON NON-SYNCHRONIZED EXOPLANETS AND IMPLICATIONS ON LIGHT CURVES

Kazumasa Ohno
Department of Earth and Planetary Sciences, Tokyo Institute of Technology, Meguro, Tokyo, 152-8551, Japan

Xi Zhang
Department of Earth and Planetary Sciences, University of California Santa Cruz, 1156 High St, Santa Cruz, CA 95064, USA

To be submitted to ApJ

ABSTRACT

Many theoretical studies of the atmospheric dynamics on exoplanets assume the synchronized rotation around their stars and succeed to reproduce the features of the observed light curves of hot Jupiters. Furthermore, recent studies have focused on the atmospheric dynamics on non-synchronized exoplanets. However, no systematic work has investigated the influence of planetary obliquity on atmospheric dynamics despite the fact that non-synchronized planets might be tilted. In this project, we systematically investigate the atmospheric dynamics on tilted exoplanets by using an idealized 2D general circulation model. Our simulations suggest that the circulation patterns on tilted exoplanets are quite different from non-tilted exoplanets but with zero eccentricity. We also predict the observable light curves. The variations of light curves for the cases of non-tilted and obliquity 90 deg are almost same. However, our predictions suggest that the peak of the light curve for the case of obliquity 90 deg happens after the secondary eclipse if the observers face to the planetary poles. Consequently, our results suggest that planetary obliquity has the significant impacts on the climates and observed light curves of exoplanets.

1. INTRODUCTION

One of the great successes of the theoretical studies for exoplanetary atmospheres is the modeling of atmospheric circulation. Previous works investigate the atmospheric circulation of hot Jupiters (e.g., Showman & Guillot 2002; Cooper & Showman 2005; Showman et al. 2008, 2009; Kataria et al. 2016; Komacek & Showman 2016), mini Neptunes, and super-Earth (e.g., Menou 2012; Kataria et al. 2014; Charnay et al. 2015), whose orbits are close to their stars. This small orbital distance causes synchronous rotation in planets by tidal dissipation, i.e., the dayside hemispheres of the planets face to their stars permanently (Guillot et al. 1996; Rasio et al. 1996). These theoretical studies for tidally locked hot Jupiters predict the super-rotating equatorial jets, which induce the eastward shifts of hotspots from the substellar point. This feature is consistent with the observed light curves of hot Jupiters that show their peaks before the secondary eclipse (e.g., Knutson et al. 2007; Showman et al. 2008; Knutson et al. 2009; Crossfield 2015).

In contrast to the tidally locked planets, atmospheric circulation of non-synchronized exoplanets were not thoroughly investigated. Planets beyond ~ 0.2 AU might not be tidally locked because the timescale of tidal spin-down is comparable to typical system ages $\sim 10^{10}$ yr if we assume sun-like stars and a Jupiter-like tidal Q value $\sim 10^5$ (Showman et al. 2015). Such non-synchronized exoplanets might have the diversity of rotation period, orbital eccentricity, orbital inclination, and planetary obliquity (the angle between the planetary rotation axis and the orbit normal), which induce complexity in theoretical studies. Showman et al. (2015) systematically explored the impacts of the relationship among rotation period, orbital period, and the radiative timescale on circulation regime with a 3D general circulation model with a non-grey radiative transfer scheme. Lewis et al. (2010), Kataria et al. (2013), and Lewis et al. (2014) also performed the 3D simulations for eccentric hot Jupiters and a mini-Neptune.

However, there has not been a systematic study that explores the influence of planetary obliquity on atmospheric circulation of exoplanets to date. The timescale of the tidal evolution of the obliquity is assumed to be comparable to the timescale of synchronization (Winn & Holman 2005), hence non-synchronized planets should be tilted.

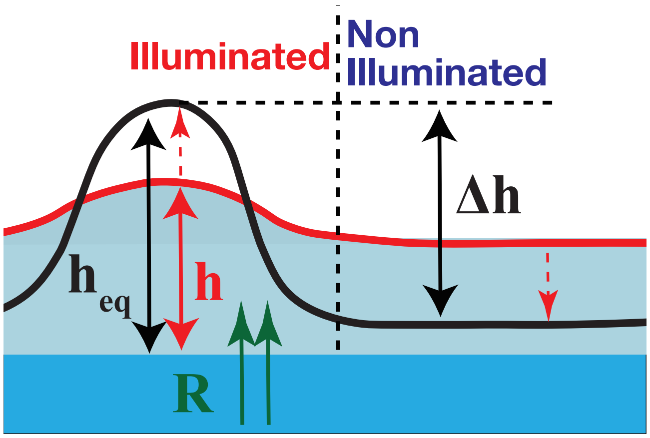

Figure 1. Schematic illustration of the one-and-a-half-layer shallow water system. We consider the upper active layer (light blue layer) and the lower quiescent layer (deep blue layer). The quiescent layer maintains the steady state, and the thickness and horizontal velocity of the active layer change with time. Radiative heating and cooling tend to restore the atmospheric thickness (red line) toward the local equilibrium value (black line). The active layer then exchanges the mass and the moment between the deeper quiescent layer (green arrow).

Langton & Laughlin (2007) investigated the spatial temperature distribution and the emergent flux of a highly tilted hot Jupiter with a 2D one-layer model. However, they also studied the case of synchronized rotation and the planetary obliquity set to 90 degree. Furthermore, their simulations failed to reproduce the equatorial eastward jet (even in the synchronized rotating case) that is suggested from the actual observations (e.g., Knutson et al. 2007, 2009).

In this study, we investigate the impacts of planetary obliquity on atmospheric circulation of non-synchronized exoplanets by using an idealized two-dimensional (2D) model. We introduce our model in Section 2. We show the preliminary results of dynamical pattern in Section 3. We then predict the observable light curves of tilted exoplanets. We present a summary in Section 4.

2. METHOD

2.1. *Shallow Water Model*

We adopt an idealized one-and-a-half-layer shallow water model to catch the feature of the atmospheric circulation of tilted exoplanets (see Figure 1). This model assumes an upper active layer that has constant density and variable height h, and a lower quiescent layer that maintains the steady state. We calculate the evolution of the height field $h(\lambda, \phi)$ and the horizontal velocity field $\mathbf{v}(\lambda, \phi)$ of the upper active layer. Such idealized 2D models have been extensively used for gas giants in our solar system (e.g., Scott & Polvani 2008), hot Jupiters (Cho et al. 2003; Showman & Polvani 2011; Perez-Becker & Showman 2013), and brown dwarfs (Zhang & Showman 2014).

The master equations of a shallow water model are given by

$$\frac{d\mathbf{v}}{dt} + g\nabla h + f\mathbf{k}\times\mathbf{v} = \mathbf{R} - \frac{\mathbf{v}}{\tau_{\rm drag}}, \tag{1}$$

$$\frac{\partial h}{\partial t} + (\mathbf{v}\cdot\nabla)h = \frac{h_{\rm eq}(\lambda,\phi,t) - h}{\tau_{\rm rad}} \equiv Q, \tag{2}$$

where λ is the longitude, ϕ is the latitude, t is the time, g is the gravitational acceleration, $f = 2\Omega_{\rm rot}\sin\phi$ is the Coriolis parameter, $\Omega_{\rm rot}$ is the angular velocity of planetary rotation, $\mathbf{k}$ is the vertical unit vector. We present the height field h as a proxy of atmospheric temperature. Especially, the second term of the left side in Equation (1) represents the pressure gradient in a shallow water model that assumes the constant density layer.

The second term of the right side in Equation (1) represents the parameterized atmospheric drag force, where $\tau_{\rm drag}$ is a characteristic timescale of the momentum dissipation of the atmosphere (Showman & Polvani 2011; Perez-Becker & Showman 2013). The drag timescale represents the many kinds of potentially important effects, which include ohmic dissipation (e.g., Perna et al. 2010) and vertical turbulence and shock (e.g., Li & Goodman 2010). Perez-Becker & Showman (2013) suggest that $\tau_{\rm drag}$ have the weaker impacts on a circulation regime than $\tau_{\rm rad}$. Therefore, we fix $\tau_{\rm drag}$ to be 10 Earth-day for simplicity in this study.

The right side of Equation (2) represents the radiative heating and cooling of atmospheres, where $\tau_{\rm rad}$ is a radiative timescale. We introduce the Newtonian relaxation (e.g., Cooper & Showman 2005; Showman & Polvani 2011; Perez-Becker & Showman 2013; Komacek & Showman 2016) of the height toward the local radiative equilibrium height $h_{\rm eq}(\lambda, \phi, t)$. This approximation allows us to perform quick simulations and the extensive explorations of the parameter space. We simply assume the radiative timescale as a free parameter in this study. The equilibrium height $h_{\rm eq}$ is calculated by the local stellar flux, therefore we define $h_{\rm eq}$ as

$$h_{\rm eq}(\lambda,\phi,t) = \begin{cases} H + \Delta h[\mathbf{r}_{\rm ss}(t)\cdot\mathbf{r}(\lambda,\phi)] & \text{when } (\mathbf{r}_{\rm ss}\cdot\mathbf{r}) \geq 0 \\ H & \text{when } (\mathbf{r}_{\rm ss}\cdot\mathbf{r}) < 0, \end{cases} \tag{3}$$

where H is the mean atmospheric thickness on the non-illuminated hemisphere (nightside), Δh is the difference of the equilibrium thickness between the substellar point and the nightside. Large value of $\Delta h/H$ corresponds to the large temperature difference between dayside and nightside, i.e., strong forcing of pressure gradient. Therefore increasing $\Delta h/H$ leads to the strong winds (Showman & Polvani 2011). We fix $\Delta h/H$ as a parameter in this study. $\mathbf{r}$ is a unit normal vector and $\mathbf{r}_{\rm ss}$ is the unit normal vector of a substellar point that moves with time. In contrast to synchronized planets, the substellar point of non-synchronized tilted planets has a more complex trajectory. The formula of $\mathbf{r}_{\rm ss}(\mathbf{t})$ is described in Section 2.2.

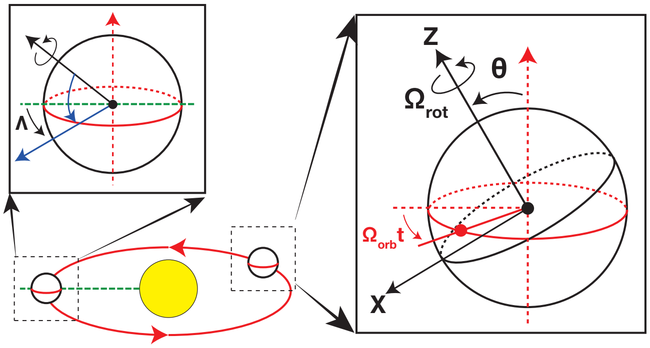

Figure 2. Illustration of the assumed system for tilted planets in this study. The red trajectory and arrow represent the orbital plane and normal, respectively. The green line and orbital normal define the plane facing to the observer. The blue line represents the rotation axis projected on the orbital plane. This coordinate sets the z-axis to be the planetary rotation axis. Planetary obliquity θ is defined as an angle between the rotation axis and the orbital normal. The Λ is defined as an angle between the blue line and the plane facing to the observer.

$\mathbf{R}$ represents the momentum transfer brought with the mass transfer from the deeper layer, and therefore this momentum transfer arises when $Q > 0$. Following Shell & Held (2004) and Showman & Polvani (2011), we describe $\mathbf{R}$ as

$$\mathbf{R} = \begin{cases} -Q\mathbf{v}/h & (Q > 0) \\ 0 & (Q < 0). \end{cases} \tag{4}$$

Note that the fluid moving out of the upper layer ($Q < 0$) should not induce the momentum transfer from upper layer, hence we expect $\mathbf{R} = 0$ when $Q < 0$. This term is crucial to reproduce the eastward equatorial jets on synchronized rotating planets (Showman & Polvani 2011).

2.2. *Time Dependence of Substellar Point*

In the case of non-tilted planets, their substellar points move along their equators. On the other hand, the substellar points move in the plane inclined from the orbital plane for tilted planets (see the right panel of Figure 2). If we assume the angular velocity of planetary rotation $\Omega_{rot} = 0$, the unit normal vector of substellar point $\mathbf{r}_{ss}(t)$ is represented by

$$\mathbf{r}_{ss}(t)|_{\Omega_{rot}=0} = \begin{pmatrix} \cos \Omega_{orb}t \cos \theta \\ \sin \Omega_{orb}t \\ \cos \Omega_{orb}t \sin \theta \end{pmatrix}, \tag{5}$$

where Ω_{orb} is the orbital angular velocity, θ is the planetary obliquity. We choose the coordinate system whose z-axis corresponds to the planetary rotation axis. To extend this formula to spinning planets, we use the rotation matrix around the planetary rotation axis. Consequently, the formula of $\mathbf{r}_{ss}$ is given by

$$\mathbf{r}_{ss}(t) = \begin{pmatrix} \cos [(\Omega_{orb} - \Omega_{rot})t] - (1 - \cos \theta) \cos \Omega_{orb}t \cos \Omega_{rot}t \\ \sin [(\Omega_{orb} - \Omega_{rot})t] + (1 - \cos \theta) \cos \Omega_{orb}t \sin \Omega_{rot}t \\ \cos \Omega_{orb}t \sin \theta \end{pmatrix}. \tag{6}$$

If we assume the limit case of $\theta = 0$, the normal vector of substellar point is represented by a following simple formula

$$\mathbf{r}_{ss}(t)|_{\theta=0} = \begin{pmatrix} \cos [(\Omega_{orb} - \Omega_{rot})t] \\ \sin [(\Omega_{orb} - \Omega_{rot})t] \\ 0 \end{pmatrix}. \tag{7}$$

2.3. *Setting of Calculations*

To solve the Equations (1)-(2) in spherical coordinates, we perform the simulation by the modified Spectral Transform Shallow Water Model (STSWM) of Hack & Jakob (1992), which introduces the spectrum transform method. A global grid is separated in 512 × 258 in longitude and latitude. We also use ∇^6 hyperviscosity to prevent the numerical instability. This model has been used for hot Jupiters and brown dwarfs (Showman & Polvani 2011; Perez-Becker & Showman 2013; Zhang & Showman 2014).

The planetary radius and the gravitational acceleration are set to $R_p = 1.2R_J = 8.2 \times 10^7$ m and $g = 21$ m s^{-2} as typical values for hot Jupiters, respectively. We set the mean geopotential gH to be 4×10^6 m^2 s^{-2} by assuming the typical pressure scale height of ∼ 200 km for hot Jupiters. The $\Delta h/H$ is set to 0.5 to reproduce the eastward jet of ∼ km s^{-1} on tidally locked hot Jupiters (Showman & Polvani 2011). We calculate the possible combinations of 0.1, 1.0, and 10 Earth days in τ_{rad}, 3.0 Earth days for the orbital period P_{orb}, 1.0 Earth days for the rotation period P_{rot}, and 0, 45, 90, 135, 180 deg for the planetary obliquity θ. We have run the simulations to 300 Earth days and make sure they have reached the steady state.

3. RESULTS

3.1. *Dynamical Pattern for Non-Tilted Exoplanets*

We firstly focus on the atmospheric dynamics on non-tilted planets to validate our model. Figure 3 shows the snapshots of the calculated height fields and eastward winds. Each distribution of the eastward winds has reached the steady state. For the case of $\tau_{rad} = 0.1, 1.0$ Earth days, the hottest point move along the equator with the period of the solar day for non-tilted planets defined by (Showman et al. 2015)

$$P_{solar} = \left| \frac{1}{P_{rot}} - \frac{1}{P_{orb}} \right|^{-1}. \tag{8}$$

The solar day P_{solar} gives the indicator of the circulation regime when compared with the radiative timescale τ_{rad}. When $P_{solar} \gg \tau_{rad}$, the large temperature difference between dayside and nightside occurs in the atmosphere and drives

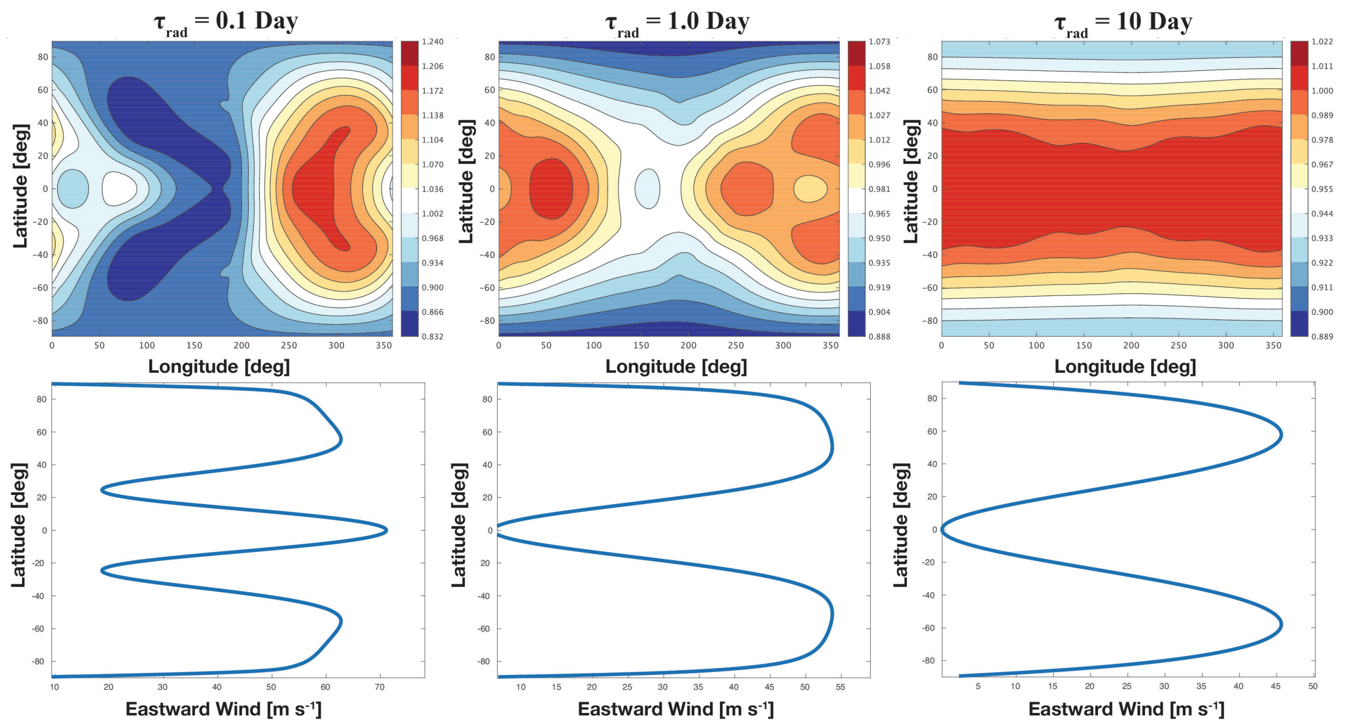

Figure 3. Spatial distribution of height field (colorscale, normalized by mean values) and eastward wind averaged for longitude. Vertical axis represents latitude. Horizontal axis represents longitude in the top rows, zonal mean eastward wind in the bottom rows, respectively. The left, middle, and right columns adopt the radiative timescale 0.1, 1, and 10 Earth days, respectively.

the eastward jet at the equator, which corresponds to the left panel of Figure 3. On the other hand, the temperature distribution is symmetric about the equator when $P_{\rm solar} \ll \tau_{\rm rad}$. In this case, the amplitude of the temperature variation is smaller than the case of short radiative timescale by an order of magnitude as we can see in the right panel of Figure 3. These results catch the basic features of circulation regime of non-tilted exoplanets suggested by previous works (see the figure 4 of Showman et al. 2015).

3.2. *Dynamical Pattern for Tilted Exoplanets*

Figures 4 and 5 show the time transition of dynamical pattern for tilted planets by assuming $\tau_{\rm rad} = 0.1$ days and 10 days, respectively. The hottest points in atmospheres periodically move within the range of $|\phi| < \theta$. As we can see in Figures 4 and 5, planetary obliquity induces the periodic heating of the high latitude regions. The period is similar to the orbital period because the time dependence of the latitude has the frequency of $\Omega_{\rm orb}$ in the Equation (6). Here we define the timescale of the transition of latitude as

$$P_{\rm lat} = P_{\rm orb}. \tag{9}$$

On the other hand, we can briefly predict the transition period of substellar point along the longitude by assuming two limit cases. First, the period takes the minimum value for $\theta = 180$ deg. And the period reaches the maximum value for $\theta = 0$ deg because the trajectory for this case should be shortest. In accordance with these limit cases, we predict the range of the transition of longitude $P_{\rm lon}$ as

$$\left|\frac{1}{P_{\rm rot}} + \frac{1}{P_{\rm orb}}\right|^{-1} \leq P_{\rm lon} \leq \left|\frac{1}{P_{\rm rot}} - \frac{1}{P_{\rm orb}}\right|^{-1}. \tag{10}$$

Here we expect that $P_{\rm lat}$ and $P_{\rm lon}$ control the circulation regime of tilted planets instead of $P_{\rm solar}$.

For the case of $\tau_{\rm rad} = 0.1$ day, the amplitude of the height field variation of highly tiled planets is $\sim 10\%$ larger than the case of the non-tilted planets. Especially, each pole experiences the strong heating when $\theta = 90$. The height fields have large differences between dayside and nightside because $\tau_{\rm rad}$ is much shorter than $P_{\rm lon}$ and $P_{\rm lat}$.

For the case of $\tau_{\rm rad} = 10$ day, the height field shows the smaller amplitude than the case of $\tau_{\rm rad} = 0.1$ day. That's because $\tau_{\rm rad}$ is much longer than $P_{\rm lon}$ and $P_{\rm lat}$, hence the region of $|\phi| < \theta$ is almost isothermal except the case of $\theta = 90$ deg. The feature of the small longitudinal variation in height field is induced by the radiative timescale longer than $P_{\rm lon}$. This feature is common in tilted and non-tilted planets.

3.3. *Prediction of Light Curve Shape*

Here we predict the shape of the observable light curves from planets. Following Zhang & Showman (2014), we integrate the height field over the hemisphere that faces to the observer as a proxy of the emergent flux from planets. Emergent flux F can be predicted by

$$F = \int_0^{2\pi}\int_0^{\pi} Eh(\phi,\lambda)(\mathbf{r}\cdot\mathbf{r}_{\rm view})\cos\phi\, d\phi\, d\lambda, \tag{11}$$

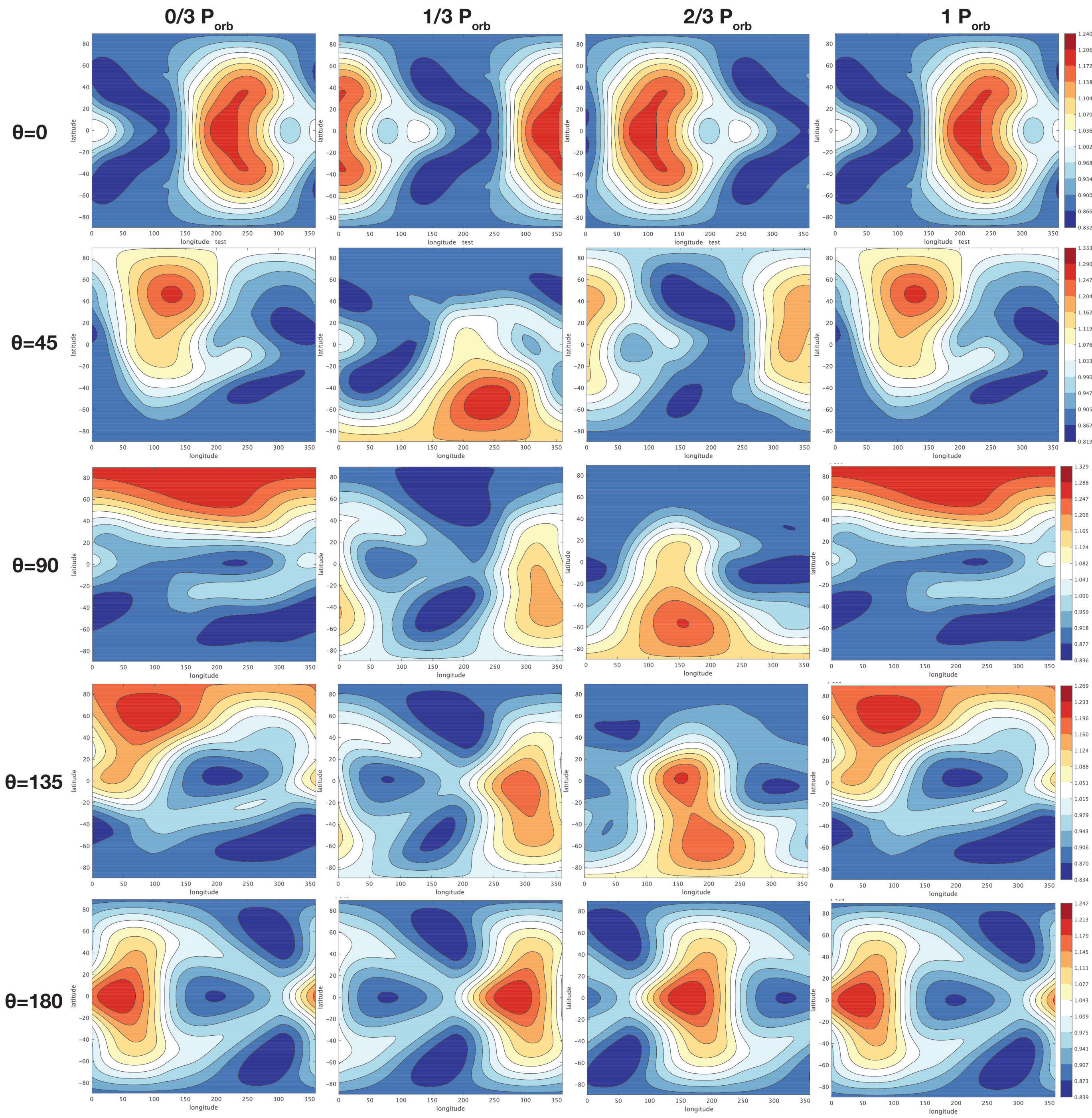

Figure 4. Spatial distributions of height field (colorscale, normalized by time averaged values). Each horizontal and vertical axises represent longitude and latitude, respectively. These series from left side to right side show the time transition of height field in an orbital period. For each simulation, the radiative timescales are set to $\tau_{\rm rad} = 0.1$ Earth day.

Where E is the function that is 1 for the case of $\mathbf{r} \cdot \mathbf{r}_{\rm view} > 0$ and 0 for the case of $\mathbf{r} \cdot \mathbf{r}_{\rm view} < 0$, $\mathbf{r}_{\rm view}$ is the point vector that is the closest to the observer. To derive the $\mathbf{r}_{\rm view}$ for tilted planets, we introduce the angle Λ related to the vernal equinox (see the left panel of Figure 2). The Λ results in the different light curve of tilted planets even in the case of same obliquity. When vernal equinox is placed to primary eclipse, Λ is set to 0 deg, i.e., the observer faces to the equator. On the other hand, Λ is set to 90 deg when vernal equinox is placed to the orbital phase 0.25, i.e., the observer faces to the pole. The longitude and latitude of $\mathbf{r}_{\rm view}$ are given by

$$\phi_{\rm view} = \sin^{-1}(\sin\theta\sin\Lambda), \tag{12}$$

$$\lambda_{\rm view} = -\Omega_{\rm rot} t. \tag{13}$$

Here $\mathbf{r}_{\rm view}$ is influenced by planetary rotation only and thus $\phi_{\rm view}$ does not depend on time.

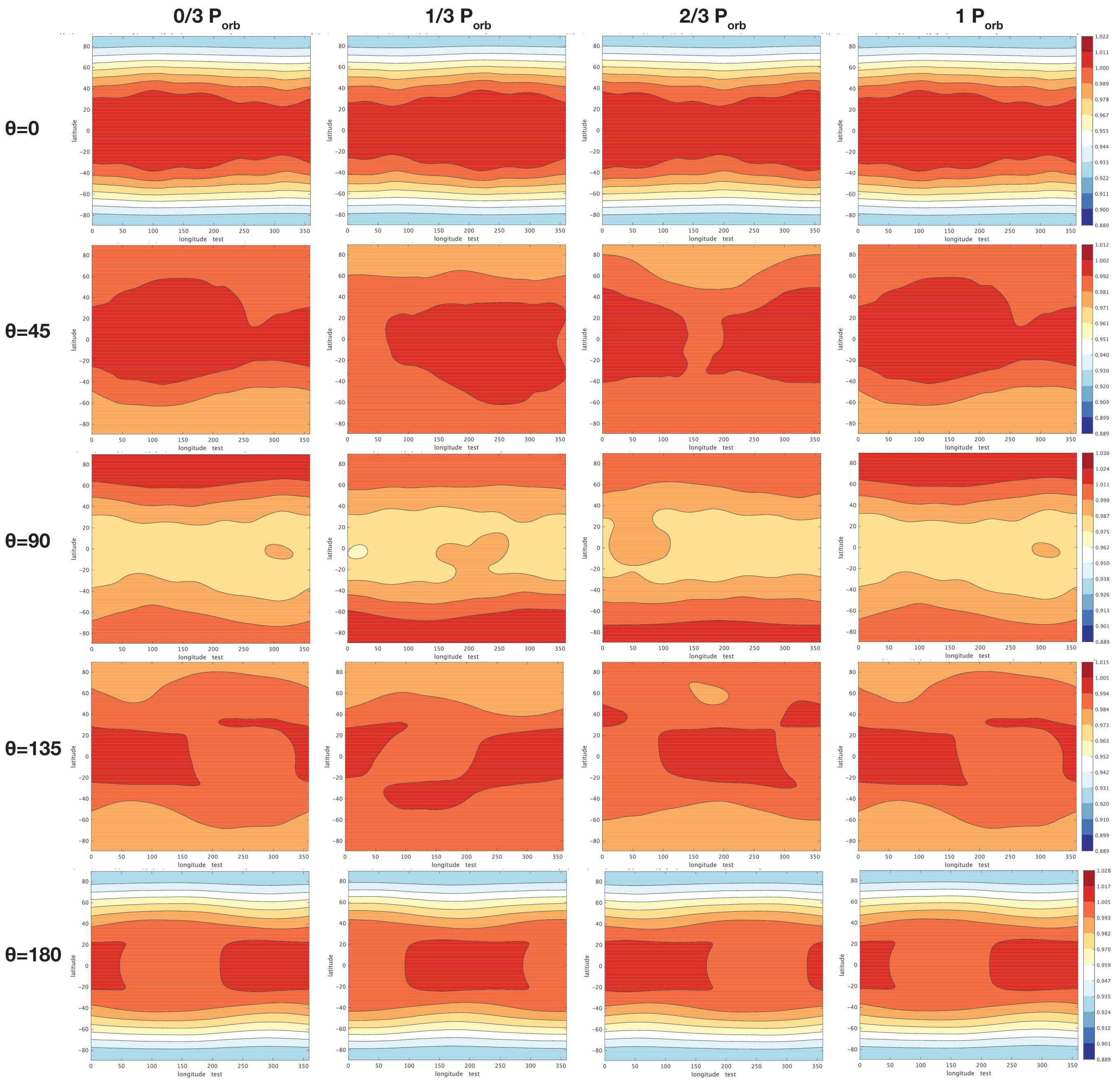

Figure 5. Spatial distributions of height field same as Figure 4. In contrast to Figure 4, each simulation assume $\tau_{\rm rad} = 10$ Earth days.

The predicted light curves are shown in Figure 6. We assume only $\tau_{\rm rad} = 0.1$ Earth days in this study because $\tau_{\rm rad}$ is predicted approximately ~ 0.2 Earth days at a semi-major axis $a = 0.2$ AU. Here the radiative timescale is predicted by (Showman & Guillot 2002)

$$\tau_{\rm rad} = \frac{Pc_{\rm p}}{4g\sigma T_{\rm e}^3}, \tag{14}$$

where P is the pressure of the heated region, $c_{\rm p}$ is the specific heat at constant pressure, σ is the Stefan-Boltzmann constant, and $T_{\rm e}$ is the equilibrium temperature given by (Guillot 2010)

$$T_{\rm e} = T_* \left(\frac{R_*}{2a}\right)^{1/2}, \tag{15}$$

where T_* is the stellar effective temperature and R_* is the stellar radius. Following Perez-Becker & Showman (2013) and Showman et al. (2015), we set $T_* = 4980$ K and $R_* = 5.5 \times 10^8$ m as the values of HD189733, $c_{\rm p} = 1.3 \times 10^4$ J kg^{-1}K^{-1}, and $P \approx 0.25$ bar.

Our predictions suggest that each light curve has the variation of 10-15%, respectively. The variation $\sim$ 15% for non-tilted planet is consistent with the previous prediction with a 3D simulation of Showman et al. (2015). We find

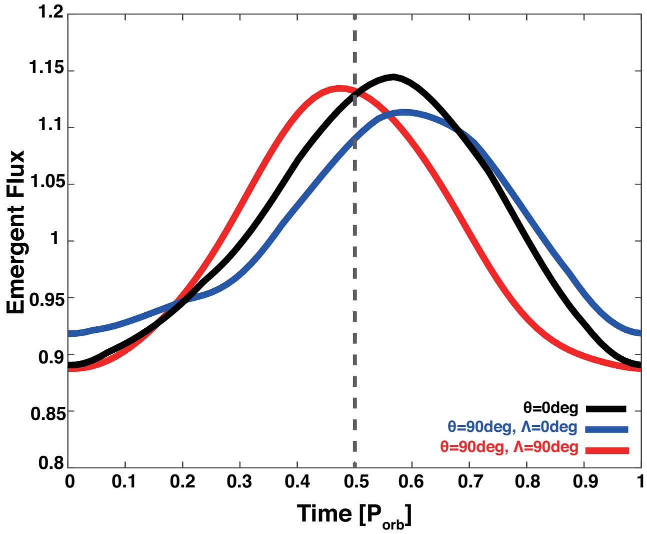

Figure 6. Emergent flux from non-tilted and highly tilted planets. The vertical axis shows the normalized flux and the horizontal axis shows the time normalized by orbital period. The black line represents the time variation of emergent flux for non-tilted planet. The red and blue lines represent for the case of $\theta = 90$ deg and $\Lambda = 0$ and 90 deg, respectively. The gray dotted lines represent the time of secondary eclipse. For these simulation, radiative timescale is set to $\tau_{\rm rad} = 0.1$ Earth days.

that the planetary obliquity has a small impact on the amplitude of the lightcurve variation. The lightcurve for the case of $\Lambda = 90$ deg has the stronger variation than the case of $\Lambda = 0$ deg because the observers face to the poles where experiment strong heating in the case of $\Lambda = 90$ deg. Our prediction also suggests that the peaks of the light curves of tilted planets happen after the secondary eclipse in the case of $\Lambda = 0$ deg. Recent observations of the *Kepler* space telescope suggest that reflective clouds located on the west side induce such phase shift (Esteves et al. 2015; Shporer & Hu 2015; Parmentier et al. 2016). However our results suggest that highly tilted planets might also cause the similar phase shift.

4. SUMMARY

We have systematically investigated the atmospheric dynamics on tilted exoplanets by using a 2D global shallow water model. Our simulations introduce the Newtonian relaxation to represent the radiative heating and cooling. Our model is able to simulate the atmospheric dynamics over a wide range of parameters, even in the planetary obliquity.

We have tested our simulations by comparing with the features of the atmospheric dynamics on non-synchronized but non-tilted exoplanets suggested by Showman et al. (2015). Our simulations reproduce the same features that are determined by the relationship of $\tau_{\rm rad}$ and $P_{\rm solar}$. For the tilted exoplanets, our simulations suggest that planetary obliquity drastically influences the dynamical pattern on the planets for the case of short and long radiative timescales, respectively. For the case of short radiative timescales ($\tau_{\rm rad} \gg P_{\rm lon}, P_{\rm lat}$), the hottest points of atmospheres periodically move within the range of $|\phi| < \theta$. On the other hand, atmosphere is almost isothermal within the range of $|\phi| < \theta$ if the radiative timescale is too long ($\tau_{\rm rad} \ll P_{\rm lon}, P_{\rm lat}$). We conclude that the relationship among $P_{\rm lat}$, $P_{\rm lon}$, and $\tau_{\rm rad}$ controls the circulation regime of tilted planets.

We have also predicted the observed light curves. Our predictions suggest that the difference of the light curve variation is small between tilted and non-tilted case. However, we find that the peak of the light curves of highly tilted planets happen after the secondary eclipse if the observers face to the equator. Such phase shifts are suggested from the recent observations with the *Kepler* space telescope. Therefore, we can expect that the future observations might help to distinguish between the non-tilted and tilted planets from such light curves.

I would like to express my deepest gratitude to Xi Zhang for many discussions and mentoring. I would also like to thank Pascale Garaud, Jonathan Fortney, and entire Kavli organizing committee for such excellent opportunity to extend the scientific field. Finally, I thank all participants who spend a lot of time in Kavli Summer Program in Astrophysics 2016. This work was supported by the Kavli Foundation, the National Science Foundation, the Other Worlds Laboratory at UCSC, and University of California Santa Cruz.

REFERENCES

Charnay, B., Meadows, V., & Leconte, J. 2015, ApJ, 813, 15

Cho, J. Y.-K., Menou, K., Hansen, B. M. S., & Seager, S. 2003, ApJL, 587, L117

Cooper, C. S., & Showman, A. P. 2005, ApJL, 629, L45

Crossfield, I. J. M. 2015, PASP, 127, 941

Esteves, L. J., De Mooij, E. J. W., & Jayawardhana, R. 2015, ApJ, 804, 150

Guillot, T., Burrows, A., Hubbard, W. B., Lunine, J. I., & Saumon, D. 1996, ApJL, 459, L35

Guillot, T. 2010, A&A, 520, A27

Hack, J. J., & Jakob, R. 1992, Description of a Global Shallow Water Model Based on the Spectral Transform Method (Boulder, CO: National Center for Atmospheric Research)

Kataria, T., Showman, A. P., Lewis, N. K., et al. 2013, ApJ, 767, 76

Kataria, T., Showman, A. P., Fortney, J. J., Marley, M. S., & Freedman, R. S. 2014, ApJ, 785, 92

Kataria, T., Sing, D. K., Lewis, N. K., et al. 2016, ApJ, 821, 9

Knutson, H. A., Charbonneau, D., Allen, L. E., et al. 2007, Nature, 447, 183

Knutson, H. A., Charbonneau, D., Cowan, N. B., et al. 2009, ApJ, 690, 822

Komacek, T. D., & Showman, A. P. 2016, ApJ, 821, 16

Langton, J., & Laughlin, G. 2007, ApJL, 657, L113

Lewis, N. K., Showman, A. P., Fortney, J. J., et al. 2010, ApJ, 720, 344

Lewis, N. K., Showman, A. P., Fortney, J. J., Knutson, H. A., & Marley, M. S. 2014, ApJ, 795, 150

Li, J., & Goodman, J. 2010, ApJ, 725, 1146

Menou, K. 2012, ApJL, 744, L16
Parmentier, V., Fortney, J. J., Showman, A. P., Morley, C., & Marley, M. S. 2016, ApJ, 828, 22
Perez-Becker, D., & Showman, A. P. 2013, ApJ, 776, 134
Perna, R., Menou, K., & Rauscher, E. 2010, ApJ, 724, 313
Rasio, F. A., Tout, C. A., Lubow, S. H., & Livio, M. 1996, ApJ, 470, 1187
Scott, R. K., & Polvani, L. M. 2008, Geophys. Res. Lett., 35, L24202
Shell, K. M., & Held, I. M. 2004, Journal of Atmospheric Sciences, 61, 2928
Shporer, A., & Hu, R. 2015, AJ, 150, 112
Showman, A. P., & Guillot, T. 2002, A&A, 385, 166
Showman, A. P., Cooper, C. S., Fortney, J. J., & Marley, M. S. 2008, ApJ, 682, 559-576
Showman, A. P., Fortney, J. J., Lian, Y., et al. 2009, ApJ, 699, 564
Showman, A. P., & Polvani, L. M. 2011, ApJ, 738, 71
Showman, A. P., Lewis, N. K., & Fortney, J. J. 2015, ApJ, 801, 95
Winn, J. N., & Holman, M. J. 2005, ApJL, 628, L159
Zhang, X., & Showman, A. P. 2014, ApJL, 788, L6